

Correlation between surface and processing parameters of an Nb-48Ti alloy produced by laser powder bed fusion additive manufacturing

Willy Ank de Morais ^{1*} 

Jhoan Sebastian Guzmán Hernández ² 

Izabel Fernanda Machado ³ 

Fernando José Gomes Landgraf ⁴ 

Abstract

The performance of engineering materials depends on the conciliation between their structure defined by the fabrication process and the properties required for their application. Within this context, the new developments in the Additive Manufacturing (AM) processes offer great potential to generate new applications and induce technological innovations with engineering materials. In this field, there are still many challenges to understanding, configuring, and controlling this new production process, which, however, has excellent potential for use in several areas, such as biomedical applications. Therefore, based on the concept of the interconnection of surface characteristics to processing parameters internal structure/properties, the present work proposed the use of profilometry results measured in cubes of the Nb-48Ti alloy previously produced by Laser Powder Bed Fusion (LPBF) to describe some aspects of its performance. Fractal dimension (D_f) and solidification front semi-angles from top surfaces in the (asymmetrical) molten pool were correlated with process parameters (E_v , energy input by volume) and structural performance (%RD, relative density). The results demonstrated the potential of using surface characterization to evaluate some process parameters of metal products obtained by LPBF.

Keywords: Additive Manufacturing; Laser powder bed fusion; Profilometry; Niobium; Molten pool; Metallurgical characterization.

1 Introduction

The Laser Powder Bed Fusion (LPBF), also known as selective laser melting (SLM), is an Additive Manufacturing (AM) process that has aroused a growing technical and scientific interest in the last years mainly for its differential advantages [1-4]: (1) obtaining complex parts, (2) minimum need of raw material (metallic powder), (3) capability to work with high melting point metals and (4) the possibility to obtain final parts without further complex steps. Figure 1 illustrates this process, which can be described as follows:

1. A laser beam at a defined velocity (v) and power (P) scans by a hatch distance (λ) a powder bed layer deposited over a table or build platform (Figure 1a) inside a chamber protected by inert gas [5:3] (Figure 1b);
2. The laser energy melts the particles present in the powder layer around the laser spot, with a portion of the solid material underneath forming a continuous solid;
3. Once a layer of the part is formed, the powder bed table (or platform) is lowered by a defined height (h), and more powder is deposited by a feed platform (Figure 1a) or tank (Figure 1b);
4. The new layer of powder is leveled by a ruler named 'recoater' (Figure 1a or 1b), and a new laser scan consolidates the next solid layer of the building product.

This process is repeated until the part is entirely built according to a predetermined scan strategy geometry imposed by directional mirrors (Figure 1a). Three main directions are customarily used as a reference system for this process [1,3,4,6]: X or scanning direction (S_D), Y or transverse direction (T_D), and Z being the building direction (B_D). An XY-scan strategy ($0^\circ/90^\circ$) sometimes leads to the S_D being equivalent to the T_D .

The range of parameters that can be used in the LPBF-AM process within which it is possible to obtain an accredited end-use product is known as the

¹Faculdade de Engenharia, Universidade Santa Cecília, UNISANTA, Santos, SP, Brasil.

²Materials Science and Engineering Department, Ohio State University, Columbus, OH, United States of America.

³Departamento de Engenharia Mecatrônica e de Sistema Mecânicos, Universidade de São Paulo, USP, São Paulo, SP, Brasil.

⁴Departamento de Engenharia Metalúrgica e de Materiais, Universidade de São Paulo, USP, São Paulo, SP, Brasil.

*Corresponding author: willyank@unisanta.br



“processing window” [1,7-9]. Traditionally, the processing window is initially defined as an optimal combination of process parameters, mainly power (P), velocity (v), hatch distance (λ), and table step lowering (h) for ‘print’, a part with lower discontinuity and high density. As described earlier, the laser must melt powder and solid material

underneath to form a continuous (bulk) part. For this, a suitable molten pool size and geometry are required. Figure 2 illustrates a typical geometry of a molten pool in LPBF, seen by three different orthogonal (XZ, XY, YZ) or process ($B_D \times S_D$, $S_D \times T_D$, $T_D \times B_D$) planes and some associated parameters, as also listed in Table 1.

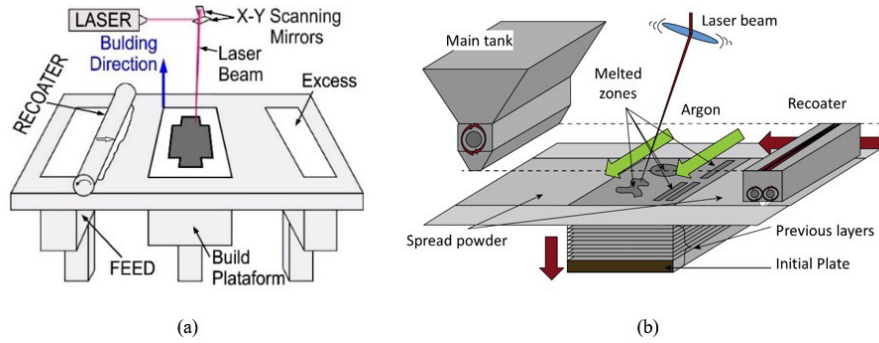


Figure 1. Schematic illustrations of the LPBF-AM process: (a) general view [3:104] and (b) more detailed [4:54].

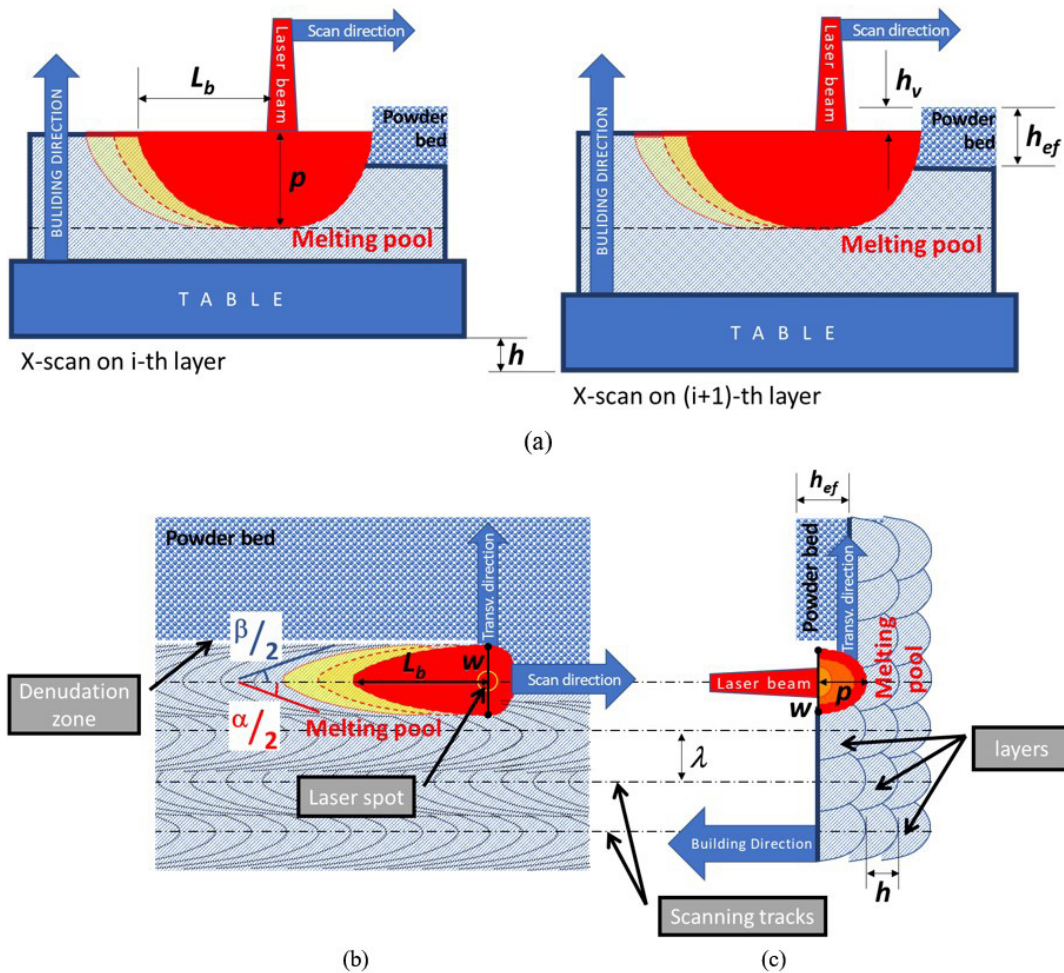


Figure 2. Schematic illustrations of the molten pool geometry in an LPBF-AM process: (a) plane XZ ($S_D \times B_D$), (b) XY plane ($S_D \times T_D$), and (c) YZ plane (or $T_D \times B_D$). The parameters shown are described in Table 1.

Figure 2 reflects the geometry and dimensions of the molten pool commonly reported by literature as in the works by Andreau et al. [10:26], Jadhav et al. [9:56], and Debroy et al. [1:151-159].

The dynamics of the molten pool surface and its solidification dictate some crucial aspects and properties of LPBF products, such as texture, as recently discussed by the present authors [11]. In one example, Dai and Gu [12] analyzed the influence of the laser energy input per unit length (*LEPUL*, or power/velocity ratio) on the molten pool behavior of SLM-processed parts, as illustrated in Figure 3. The authors concluded that the applied *LEPUL* plays a crucial role in determining the surface quality of LPBF products due to its influence over the molten pool. Observing the profile

of the molten pool shown in Figure 3, one can observe the evolution of surface roughness with increasing energy: initially decreasing from very rough (Figure 3a) to smooth (Figure 3c) and subsequently rising to rough again (Figure 3d).

Works as Dai and Gu [12] (Figure 3), Jadhav et al. [8], Mostafaei et al. [13], and Andreau et al. [10] indicate that surface characteristics, fabrication parameters, and thus properties of LPBF are all interconnected. This is an important implication, as it justifies using surface analysis of LPBF products as an alternative for their (bulk) characterization. This characterization is crucial to understanding their final performance as the LPBF process involves many variables, conditions, and parameters that can influence the results obtained [1,4,7,14].

Table 1. Some critical parameters for LPBF

	Type of dimension and description	Observable plane		
		XY	XZ	YZ
Molten pool main dimensions	L_b - molten pool length back or 'tail length'	•	•	-
	$\alpha/2$ and $\beta/2$ - solidification front semi-angles from the top surface	•	-	-
	w - molten pool width	•	•	-
	d - molten pool depth	-	•	•
Process dimensions	λ - distance between laser scanning tracks or hatch distance	•	-	•
	h - table step lowering or apparent layer height	-	•	•
Powder-related dimensions (*)	h_{ef} - real powder height, associated with the powder's specific gravity	-	•	•
	h_v - powder to solid surface height variation (due to the loss of interparticle voids after melting)	-	•	•

(*) Observation: $h_{ef} = h/d_{\text{powder}}$, where d_{powder} is the Specific Gravity of the powder about the bulk material, including the voids between powder particles (powder apparent density), that disappear with adequate laser melting [15].

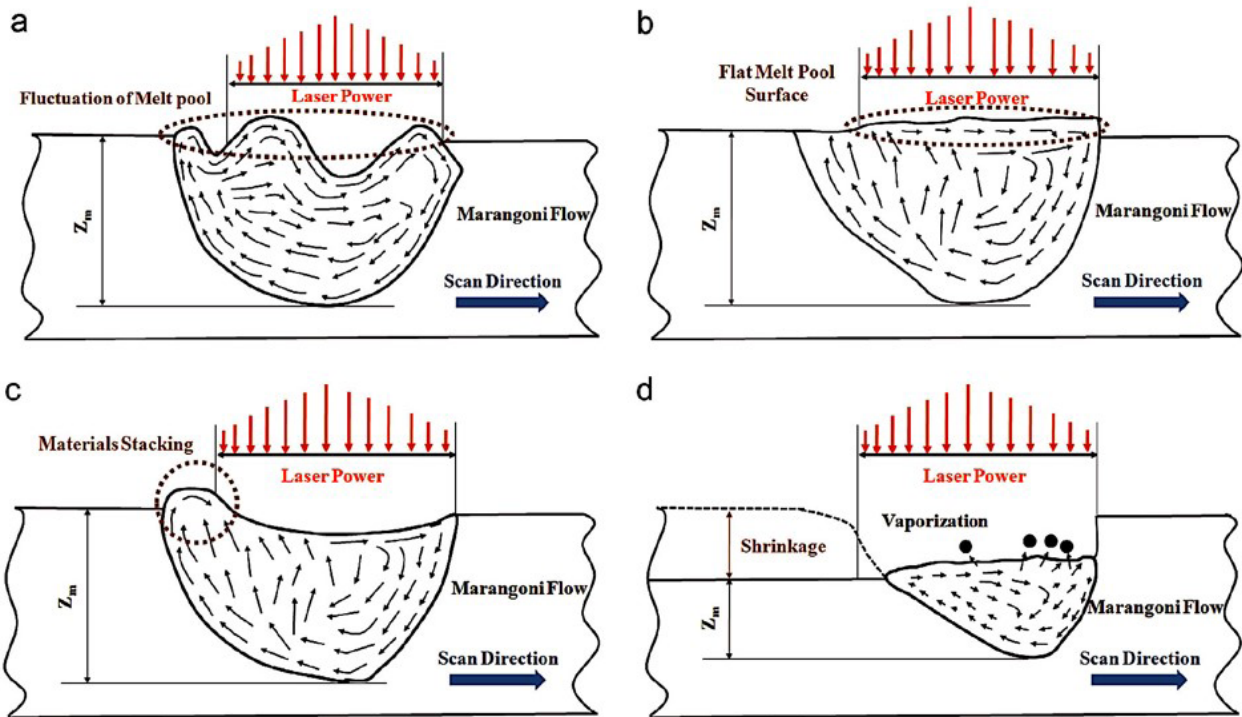


Figure 3. Schematics of the change in cross-sections along the laser scan direction of the molten pool during SLM (equivalent to LPBF) process of TiC/AlSi10Mg powder by ytterbium fiber laser on increasing P/v ratio or *LEPUL*: (a) 375 J/m; (b) 500 J/m; (c) 750 J/m; and (d) 1500 J/m [12:105].

Based on the concept of the interconnection between surface characteristics and internal structure/properties, it is proposed to use profilometry results measured in cubes of Nb-48Ti alloy produced by the LPBF to describe some aspects of their internal structure. General results such as fractal dimension (D_f) or more specific measurements such as solidification front semi angles from top surfaces in the (asymmetrical) molten pool end were correlated with process parameters (E_v , energy input by volume) and structure characteristic (%RD, relative density).

2 Materials and methods

2.1 Materials

The specimens were built using Nb-48Ti alloy, a promising candidate for use in biomedical applications [16,17]. The raw material was a plasma atomized spherical powder ($D_{50} = 31 \mu\text{m}$) supplied by Advanced Powder and Coating Company with the chemical composition listed in Table 2. The specimens were built as $10 \times 10 \times 10 \text{ mm}^3$ cubes by LPBF Concept Laser M2 Cusing system at the SENAI Innovation Institute for Manufacturing Systems and Laser Processing (Joinville, SC), operated using Nd:YAG Laser, with a wavelength of 1.075 nm, and fixed laser beam diameter of $50 \mu\text{m}$. Further material and building data are described elsewhere [18-20].

The most crucial manufacturing parameters used and results obtained were [15,18-20]:

- use of an “island” $5 \times 5 \text{ mm}^2$ X-Y scanning strategy where each layer had the scanning direction reversed (‘chessboard’ strategy), as illustrated in Figure 4
- scanning direction (S_D) is equivalent to transverse direction (T_D);
- adoption of a hatch distance $\lambda=105 \mu\text{m}$, and table step lowering $h=30 \mu\text{m}$;
- use of laser power $P = 150, 200, 250,$ and 300 W , and scanning velocity $v = 900, 1000, 1100, 1200, 1300,$ and 1400 mm/s ;
- obtained range of relative density $\%RD = 95.7$ to 99.8% ($\rho = 5.74$ to 5.99 g/cm^3) [20];
- a ‘process window’ zone defined when $\%RD \geq 99.4\%$;
- specimens formed by 335 layers;
- energy input by volume $E_v = 34$ to 95 J/mm^3 as described by Equation 1 [1,9,11,12]

$$EV = 106 \cdot LEPUL / (\lambda \cdot h) = 106 \cdot P / (v \cdot \lambda \cdot h) \quad (1)$$

Where: P (W) is power, v (mm/s) is scanning velocity, λ (μm) is the width between lanes or hatch distance, and h (μm) is the table step lowering that defines E_v (J/mm^3). $LEPUL = P/v$ (J/mm) is the laser energy input per unit length, as formerly cited [12].

Table 2. Chemical composition of Nb-48Ti starting powder, as supplied by the manufacturer (wt.%) [18]

Nb%	Ti%	Ta%	Fe%	%C	Cr%	Al%	Si%	%Ni, %Cu
51.9	48	0.1235	0.0060	0.0035	0.0027	0.0012	0.0010	< 0.0005

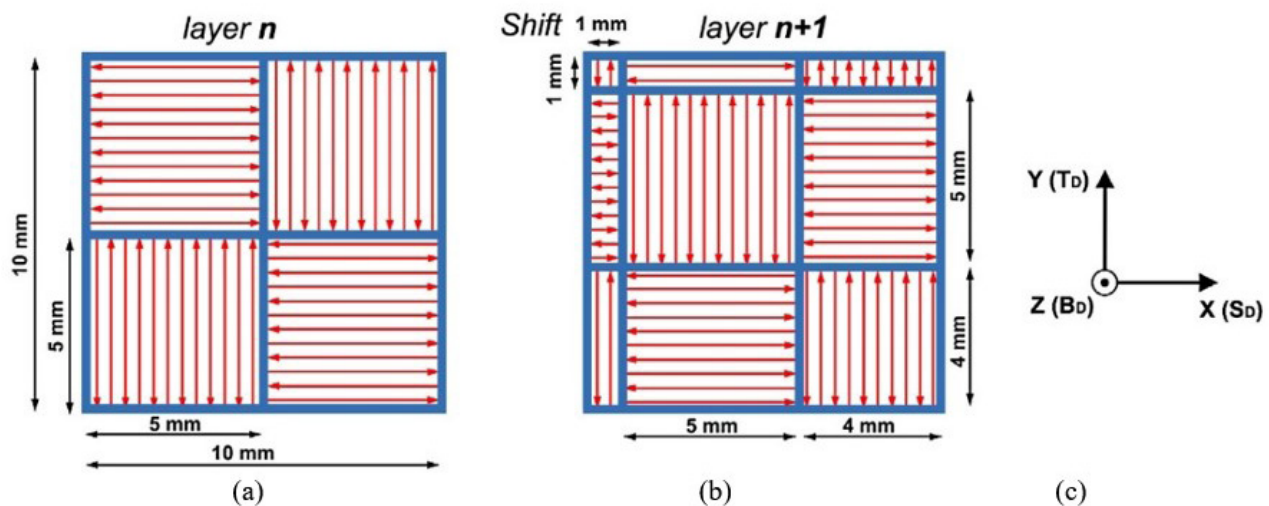


Figure 4. Schematic illustration of laser scanning strategy adopted. (a) Layer n: chessboard strategy. (b) Layer n+1: chessboard strategy with 90° rotation with 1 mm shift at the Y and X axes. (c) Reference coordinate system. The thick blue lines are the ‘island contours’ [20:487].

2.2 Methods

A non-contact Taylor Hobson 3D optical profiler was used to observe and characterize the top surfaces of the samples. This device uses coherence correlation interferometry (CCI) to obtain high-resolution images even on irregular surfaces. After examined the applicability of the surface characterization parameters offered by the equipment, two were chosen: Fractal dimension (D_f by enclosing boxes method) and the semi-angles of the surface molten pool front ($\alpha/2$ and $\beta/2$, Figure 2b). It was expected that these parameters are associated with the solidification dynamics of the molten pool, with D_f being related to the stability of the pool surface and the angles with how the solidification front consolidates. The profilometry results were compared with the following parameters: relative density ($\%RD$), volumetric energy input (E_v), and transversal molten pool size (YZ plane, Figure 2c).

The results obtained from profilometry analysis were compared to images generated with a FEI Inspect™ F50 Field Emission Gun Scanning Electron Microscopy (FEG-SEM) operated at 20 kV acceleration. Each sample was analyzed on the top surface in an area of $850 \times 850 \mu\text{m}^2$ between the edges of the scan “islands”, represented by the blue lines in Figure 4. This condition was necessary because at the border of each “island” the laser is not turned off, which introduces more energy and typically a “keyhole mode” condition, changing the behavior of the molten pool in that region [20:486].

Furthermore, metallographic analysis was used to obtain the molten pool dimensions, using YZ sections of all samples in the last deposited layer to avoid remelting distortions [18,21,22]. These data were analyzed by the MiniTab software to generate interpolation equations as a function of P and v . Using this information, it is possible to quantify the overlap ratio ($\%O_vR$) on TD (Y, Figure 2) as described by Equation 2 [23-25]:

$$\%O_vR = 100(w - \lambda) / w \quad (2)$$

Where: w (μm) is the width of the molten pool, and λ (μm) is the hatch distance.

The track-by-track deposition of metal powders yields overlapping when the previous solid material is molten and re-solidified [13,26]. A minimum value of $\%O_vR$ (or E_v) ensures that all points have been melted at least once, and specific values can provide material-specific properties [13].

Overlapping of molten pools is a crucial LPBF-AM process characteristic associated with several properties of their products like density/porosity [1,7,13,24], surface roughness [2,9,13,21,24], and even crystalline texture [6,10,11,21,26].

3 Results and discussion

3.1 Molten pool dimensions

Figure 5 shows some micrographs of YZ section used to determine molten pool dimensions in the last deposited layer, as highlighted and indicated by a thin arrow. Even in this position, usually, it is not possible to observe the total width (w) of the molten pool (Figure 5d). In this case, the half width ($w/2$) is measured, and a symmetrical geometry is assumed to obtain w [8,18].

A molten pool deeper and wider than the others, related to the island contour (Figure 4), can be seen in the micrograph of the specimen obtained with $P=300$ W and $v=1300$ mm/s, as dash highlighted and indicated by a thick arrow in Figure 5c.

The direct numerical results from molten pool measurements are presented in Figure 6. The interpolation equations obtained were Equation 3 and Equation 4, graphically illustrated in Figure 7:

$$d = -265.642 + 0.201912(v) - 0.00151717(Pv) + 2.37452(P) \quad (3)$$

$$w = 38.8726 + 0.0177671(v) - 0.000441013(Pv) + 0.816891(P) \quad (4)$$

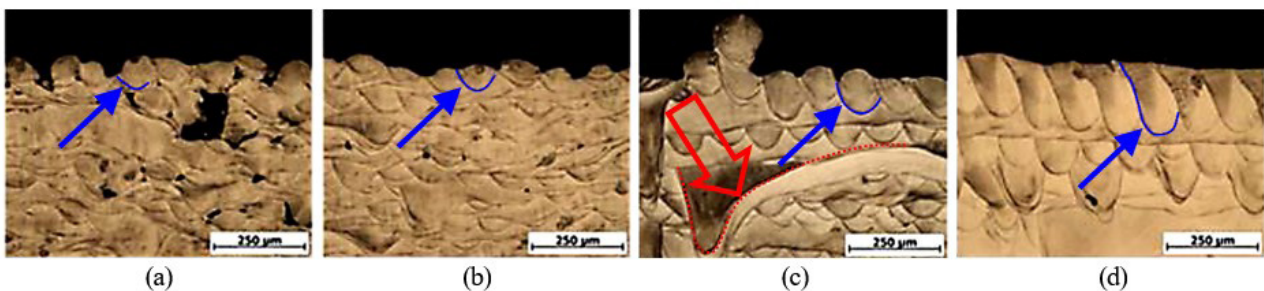


Figure 5. Micrographs of YZ sections used to determine molten pool dimensions for: (a) $P=150$ W, $v=1300$ mm/s ($E_v = 36.6$ J/mm³); (b) $P=150$ W, $v=1000$ mm/s ($E_v = 47.6$ J/mm³); (c) $P=300$ W, $v=1300$ mm/s ($E_v = 73.3$ J/mm³); and (d) $P=300$ W, $v=1000$ mm/s ($E_v = 95.2$ J/mm³) (samples etched with Kroll reagent).

The results show depth (d) and width (w) as directly proportional to power (P) and inversely proportional to scanning velocity (v), with depth being more sensitive than width, which agrees with the literature [8,18,21,27]. Inside the ‘process window’ zone (i.e., $\%RD \geq 99.4\%$), the ratio of molten pool dimensions interpolated (w and d) to LPBF process dimensions (λ and h , Table 1) were: $w/\lambda = 1.24 \pm 0.08$, and $d/h = 3.6 \pm 0.5$. The latter is much higher than the threshold values, reported by literature as required for complete melting between layers along B_D , i.e. 0.6 to 2.0 [1,4]. The molten pool aspect ratio was $w/d = 1.22 \pm 0.1$, which is lower than the values typically expected for the conduction mode (3 to 4), indicating a keyhole transition mode condition as shown in Figure 5d [1,10,21,27]. These results suggest that the molten pools observed are typically deep and, thus, reinforce the importance of analyzing their overlapping in the TD direction, as described by Equation 2.

3.2 Surface characteristics

Figure 8 presents the results of profilometry maps. A trend of increasing roughness with decreasing power and increasing scanning velocity can be noted. In other words, the lower the laser energy input, the lower the surface roughness, as observed in the literature [21,24]. This behavior is expected since less overlap ($\%O_vR$) between TD neighboring melt pools impairs the continuity of the solid material (lowering $\%RD$) and its smoothness (increasing D_f) [12,28].

Figure 9a shows the expected correlation between volumetric energy (E_v) and relative density ($\%RD$), an internal characteristic of the samples. The ‘process window’ zone is defined by an optimum E_v range ($63 < E_v < 75 \text{ J/mm}^3$) to obtain a highly dense LPBF product ($\%RD > 99.4\%$), as indicated by the rectangle in Figure 9a. The same trend can be seen with roughness as traduced by fractal dimension (D_f) and as shown in Figure 9b.

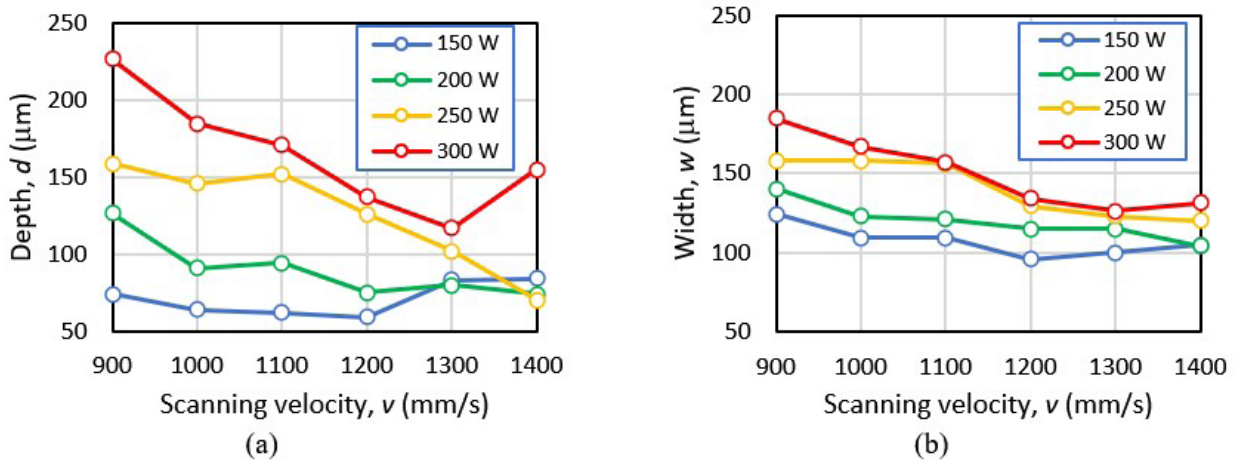


Figure 6. Molten pool dimensions measured for all combinations of power (P) and scanning velocity (v) (a) depth, and (b) width.

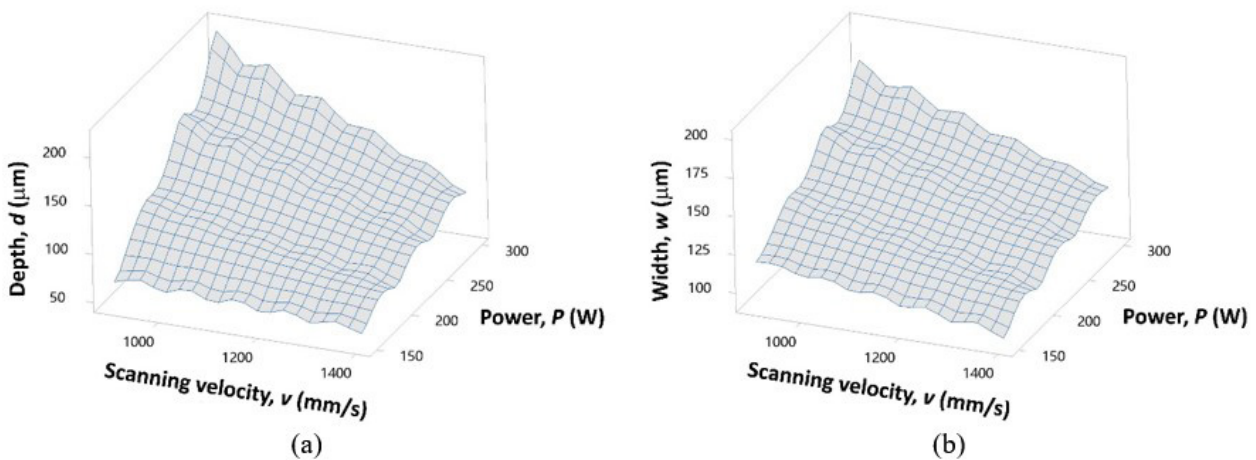


Figure 7. Molten pool dimensions interpolated as a function of power (P) and scanning velocity (v): (a) depth by Equation 3, and (b) width by Equation 4.

Although it seems that increasing volumetric energy (E_V) improves surface quality by reducing the lack of fusion defects and their associated impact on surface roughness, it is known that excessive E_V led to the formation of other types of internal (e.g., gas entrapment, keyhole porosities) and external defects (e.g., spatter) which impairs surface quality [1,8,10,12,28]. This trend is highlighted in both graphs in Figure 9 by dashed ellipses where higher E_V values worsen the material's continuity (%RD) and roughness (D_f).

Remarkably, results in Figure 9b show that the best condition occurs just before the lowest surface roughness, equivalent to an intermediate state between “b” and “c” in Figure 3 [12].

Figure 10 presents some details of profilometry measurements of the selected samples shown in Figure 5. In this case, the surfaces were taken from 4 different extreme conditions of % $O_V R$ to demonstrate the behavior of molten pools' front borders at XY plane (Figure 2b).

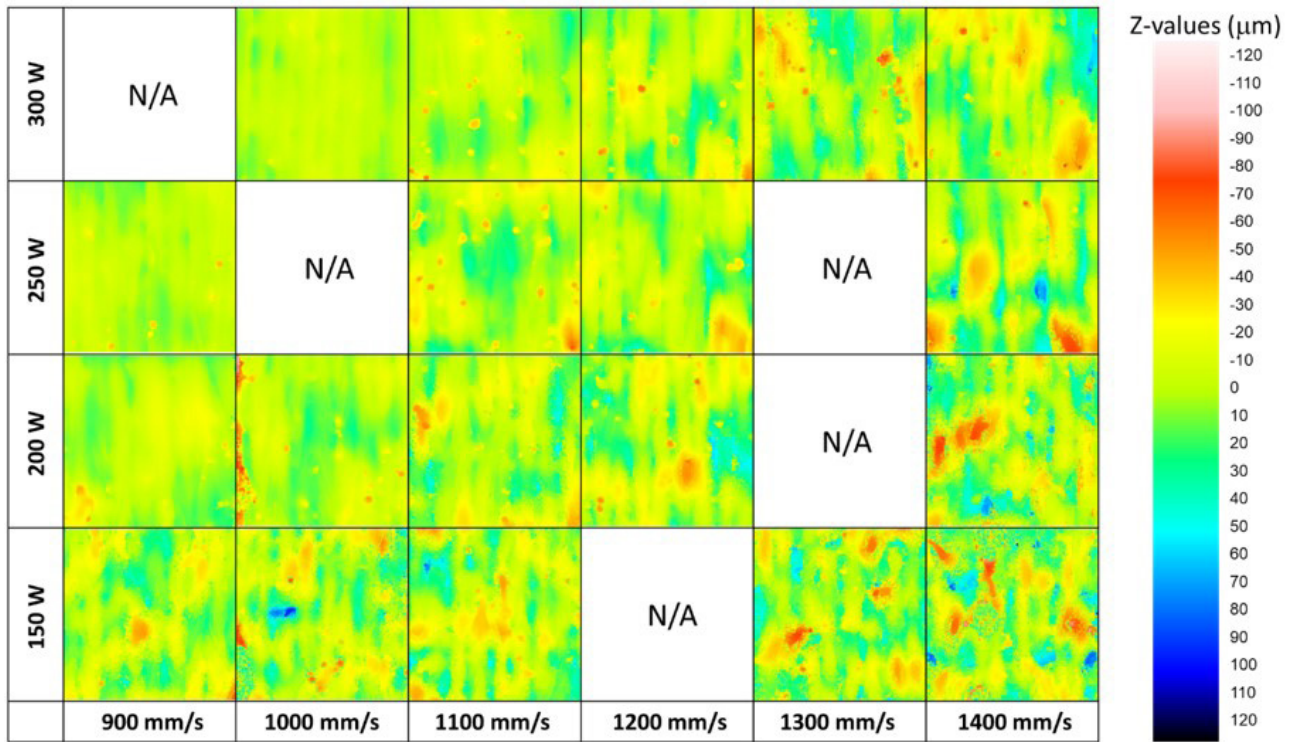


Figure 8. 3D profilometry maps obtained from an 850 x 850 μm^2 surface of the samples (N/A = not available).

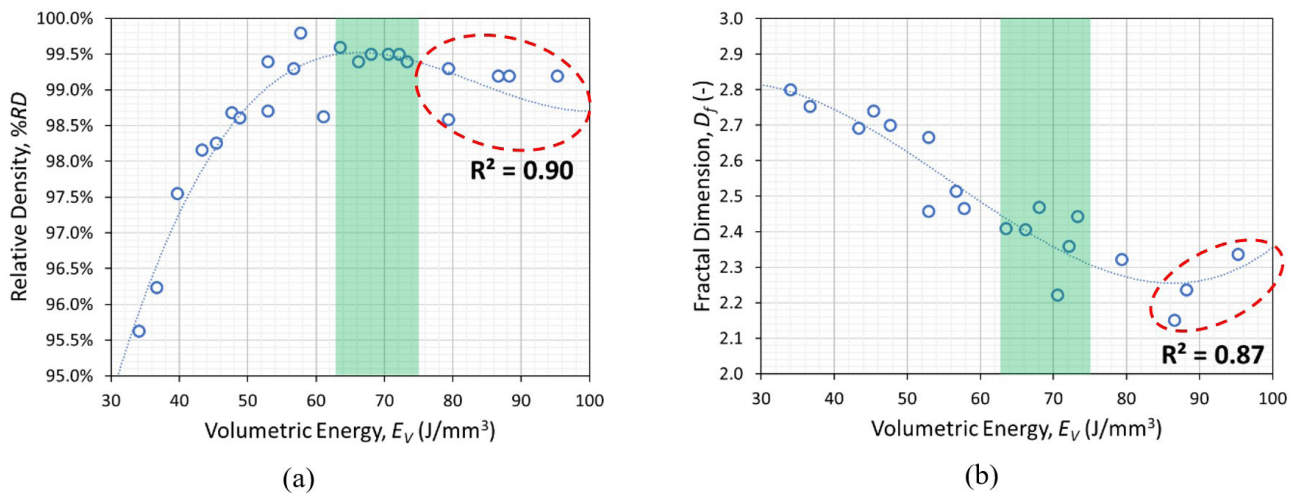


Figure 9. Effect of volumetric energy (E_V) on: (a) relative density (%RD), and (b) fractal dimension (D_f). The rectangle indicates the ‘process window’ zone and 3rd-degree polynomial fit was used for both datasets.

It can be noticed how the geometry of the solidification front is reflected by its semi-angle values ($\alpha/2$ and $\beta/2$). In this case, the only sample within the ‘process window’ is shown in Fig. 10c and presents a molten pool XY angle ($\alpha/2 + \beta/2$) = 29° .

Figure 11a presents the values of solidification front semi-angles of the molten pools’ top surface (on XY plane, Figure 2b). Additionally, Figure 11b presents the correlation between the values of overlapping ratio ($\%O_vR$), as calculated using Equation 2 and Equation 4, and the volumetric energy (E_v). In both figures the range of the ‘process window’ zone (i.e., $63 < E_v < 75 \text{ J/mm}^3$, or $\%RD \geq 99.4\%$) is highlighted.

The ‘process window’ is associated with a molten pool solidification front angle range of $24 < (\alpha/2 + \beta/2) < 33^\circ$ and an overlapping range of $18 < \%O_vR < 26\%$.

Figure 11a shows that the molten pools formed in asymmetric conditions as their semi-angles differ, especially at higher energy levels (E_v). Andreau et al. [10] discussed this situation, explaining that one side of the molten pool is in contact with the solidified metal from the previous track (Figure 2b); as this solid metal has a thermal conductivity (κ) of about 100 times higher than the loose powder, it leads to asymmetrical isothermal [10] and thermal gradient (G) [26] distribution in the molten pool.

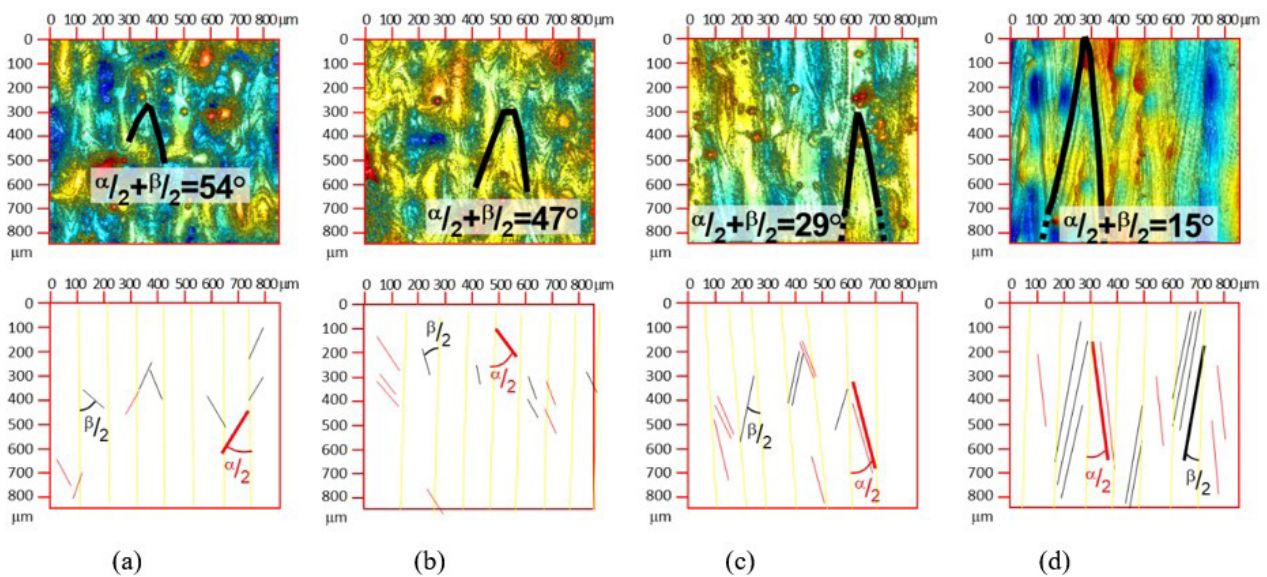


Figure 10. The top surface of selected Nb-48Ti LPBF-AM samples showing their molten pool front semi-angles ($\alpha/2 + \beta/2$) as registered by profilometry in the following conditions: (a) $P=150 \text{ W}$, $v=1300 \text{ mm/s}$; (b) $P=150 \text{ W}$, $v=1000 \text{ mm/s}$; (c) $P=300 \text{ W}$, $v=1300 \text{ mm/s}$; and (d) $P=300 \text{ W}$, $v=1000 \text{ mm/s}$.

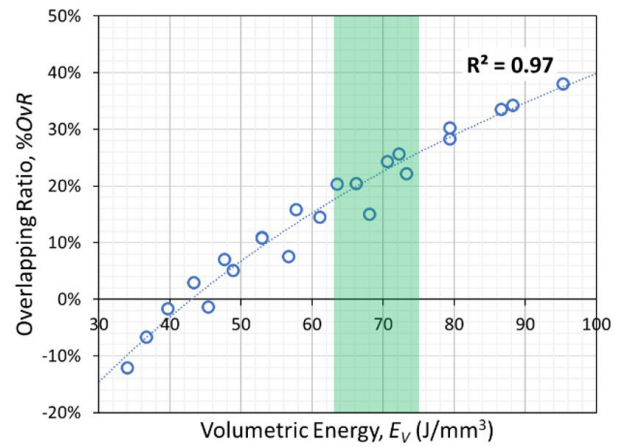
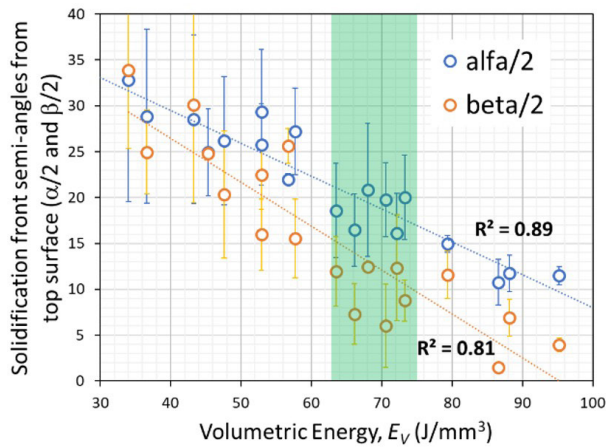


Figure 11. Effect of volumetric energy (E_v) on: (a) solidification front semi-angles ($\alpha/2 + \beta/2$) on XY plane, and (b) overlapping ($\%O_vR$) (linear fit for (a) and 2nd-degree polynomial fit for (b)).

Thus, the molten pool formed on the previously overlapped trackside has a wider solidification front, favored by the greater thermal conductivity of the solid metal present. As the amount of the solid metal present (or near) this side of the track is proportional to $\%O_vR$ (and to E_v), this leads to a larger semi-angle ($\alpha/2$) on this side in comparison to the semi-angle ($\beta/2$) on the other side, both correlated to $\%O_vR$ or E_v as represented in Figure 12. It can be noted that the scenario is valid even in unusual conditions when there is or is not solid metal on both sides of the track (i.e., $\%O_vR < 0\%$ or $\%O_vR > 100\%$), as there will always be an asymmetrical distribution of solid metal already molten around scan track.

Figure 13 shows the correlation between internal characteristic of the samples ($\%RD$) and external morphological parameters (D_f , $\alpha/2$ and $\beta/2$). Within the ‘process window’ zone (i.e., $\%RD \geq 99.4\%$) the following average values were obtained: $D_f = 2.4 \pm 0.12$; $\alpha/2 = 21 \pm 4,8^\circ$, and $\beta/2 = 11 \pm 3,6^\circ$. It is noting that the averages obtained were well-defined values across the entire range, as typically occurs for E_v values [18,21,24,29]. Thus, the results in Figure 13a indicate the possibility of using the $\%RD$ versus D_f relationship to monitor the LPBF process based on its surface aspect.

Considering that the overlapping of the molten pool has been identified as a way of controlling the type of solidification front [30] and the crystalline texture [31], the measurement of $\alpha/2$ and $\beta/2$ can be useful to perform this control as well.

Figures 14 to 17 show schematic representations of molten pool borders on top surfaces with their equivalent SEI-SEM images. In this case, the same conditions shown in Figure 10 were used, as summarized in Table 3. The molten pool geometry was derived from profilometry results described elsewhere [32]. In these representations, all dimensions are proportional to the real value and, to simplify the description, only the XX scan and the conduction mode for the molten pools were considered; that is, molten pools were considered as simple parabolic geometry.

The inhomogeneity and asymmetry of the real molten pools, as can be seen by the micrographs in Figure 5, were not considered in this analysis as well the presence of “keyhole mode” condition (see Figure 5d and its discussion). Both situations could generate incorrect energy considerations in the formation and dynamics of the weld pools and their related characteristics. These issues were partially discussed elsewhere [32] and are under investigation by the present authors.

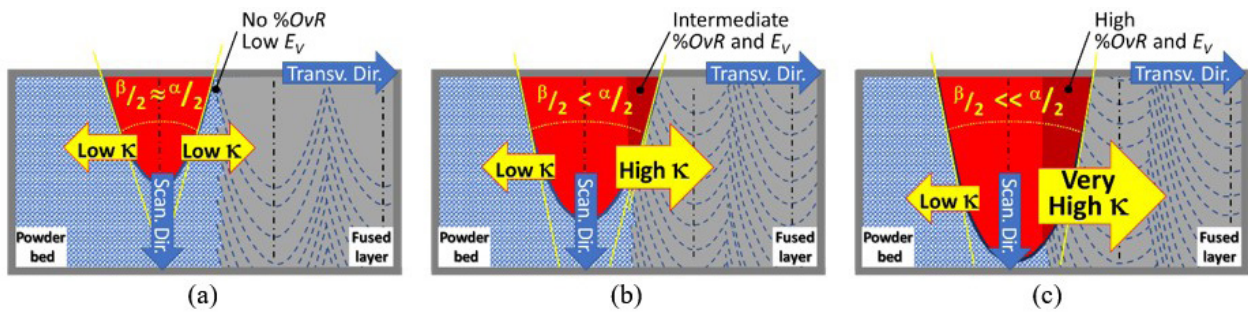


Figure 12. Schematic representation of the thermal conductivity (κ) effect on solidification front semi-angles ($\alpha/2 + \beta/2$) on XY plane according three conditions of $\%O_vR$ or E_v : (a) without, (b) low, and (c) high level of $\%O_vR$. The dot-dash lines represent the laser track centerline associated with a constant hatch distance (λ).

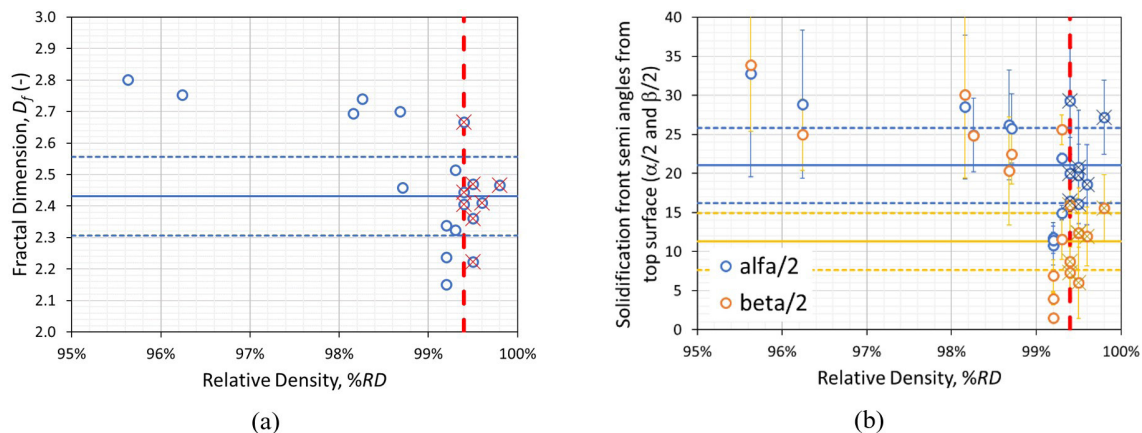


Figure 13. Effect of relative density ($\%RD$) on: (a) fractal dimension (D_f), and (b) solidification front semi-angles ($\alpha/2 + \beta/2$) on XY plane. The lines indicate: the average values (horizontal solid), 95% confidence (horizontal dashed), and the limit of the ‘process window’ zone (vertical dashed) within the “X” marked data were obtained.

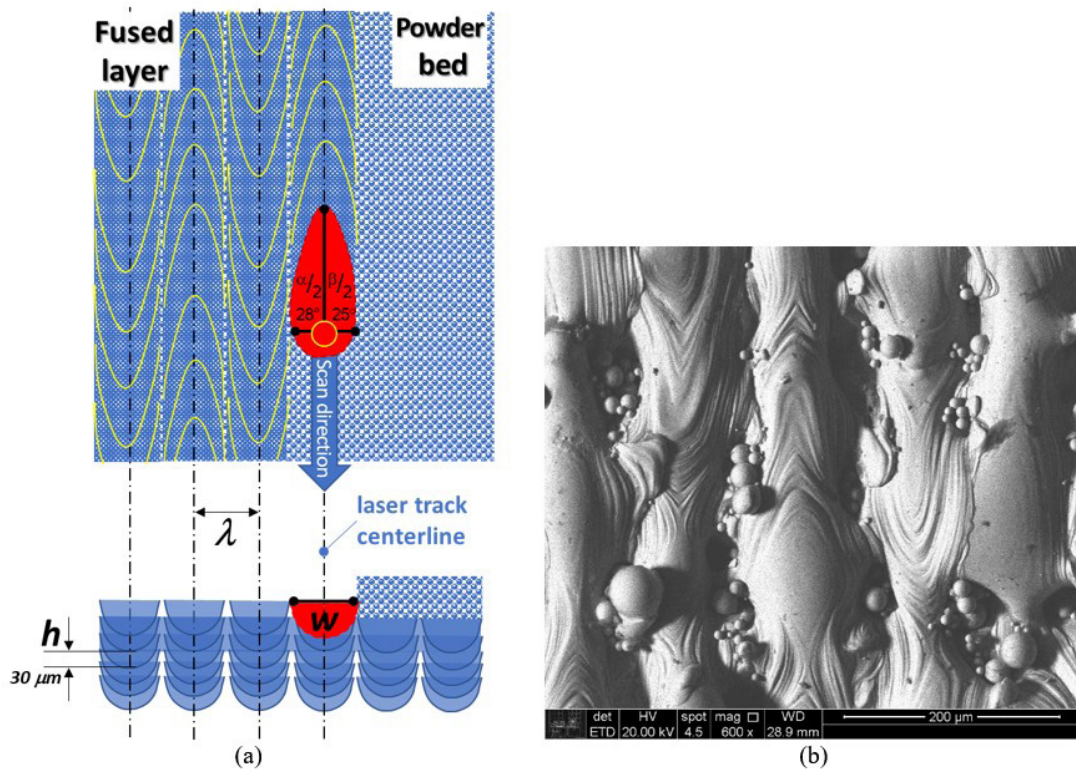


Figure 14. Molten pools geometry in the XY plane (or $S_D \times T_D$): (a) schematic, and (b) as registered by SEI-SEM. Conditions: $P=150$ W, $v=1300$ mm/s, and $E_v=36.6$ J/mm³; $\%O_vR = -6.6\%$ (see Table 3).

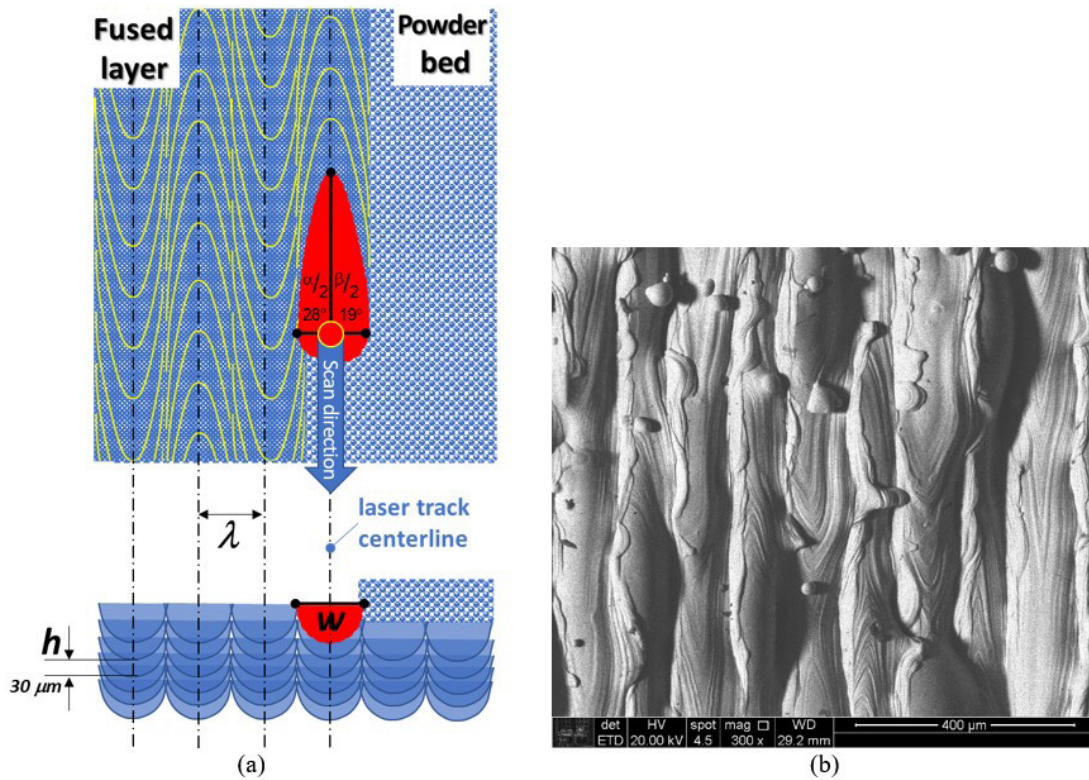


Figure 15. Molten pools geometry in the XY plane (or $S_D \times T_D$): (a) schematic, and (b) as registered by SEI-SEM. Conditions: $P=150$ W, $v=1000$ mm/s, $E_v=47.6$ J/mm³; $\%O_vR = 7.1\%$ (see Table 3).

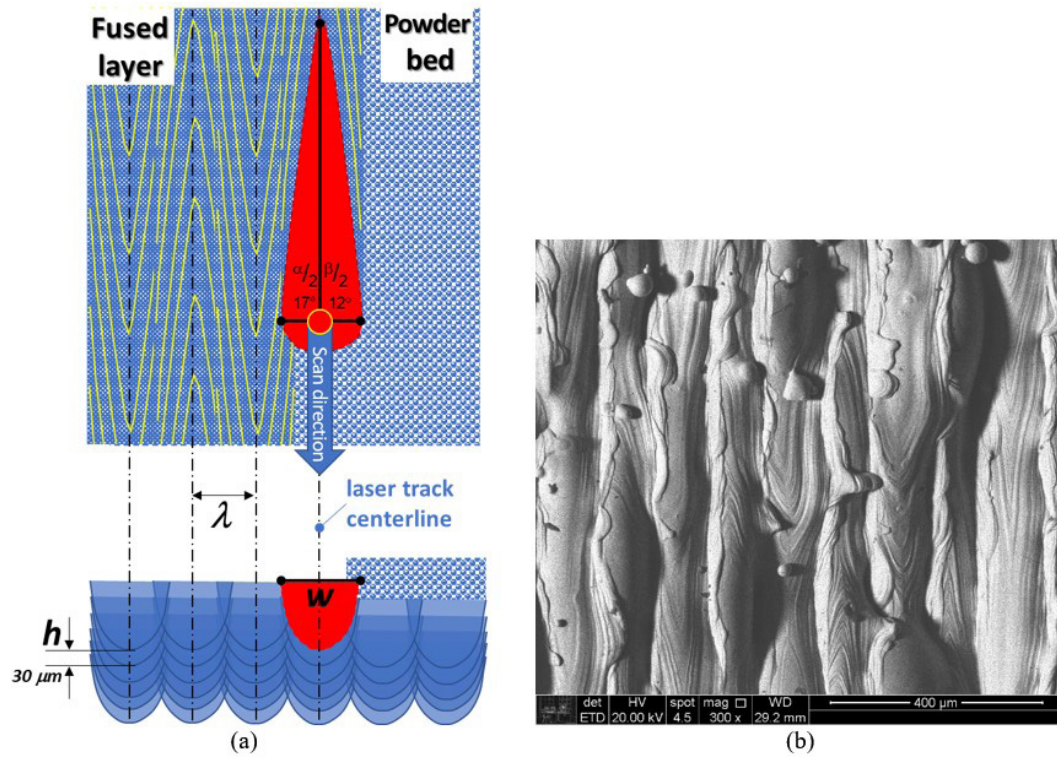


Figure 16. Molten pools geometry in the XY plane (or $S_D \times T_D$): (a) schematic, and (b) as registered by SEI-SEM. Conditions: $P=300$ W, $v=1300$ mm/s, $E_v=73.3$ J/mm³; % $O_R = 22\%$ (see Table 3).

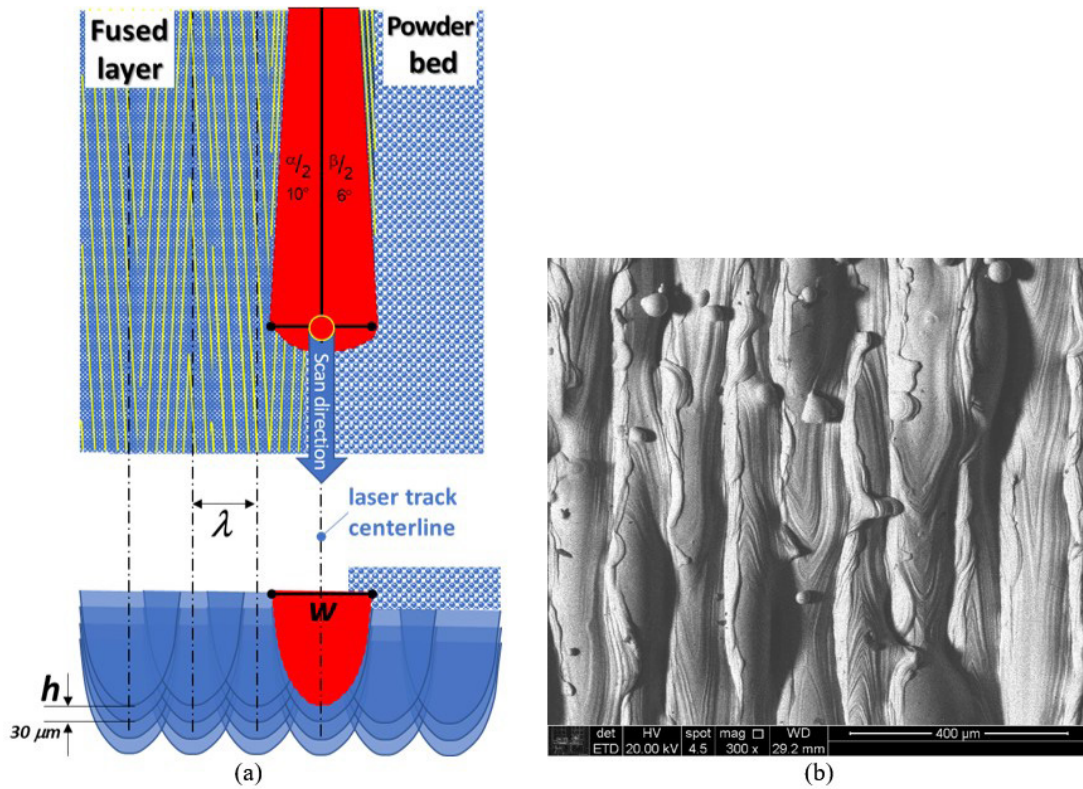


Figure 17. Molten pools geometry in the XY plane (or $S_D \times T_D$): (a) schematic, and (b) as registered by SEI-SEM. Conditions: $P=300$ W, $v=1000$ mm/s, $E_v=95.3$ J/mm³; % $O_R = 38\%$ (see Table 3).

Table 3. General results from molten pool measurements and profilometry parameters

Parameter	$P=150\text{ W}; \nu=1300\text{ mm/s};$ $E_v = 36.6\text{ J/mm}^3$	$P=150\text{ W}; \nu=1000\text{ mm/s};$ $E_v = 47.6\text{ J/mm}^3$	$P=300\text{ W}; \nu=1300\text{ mm/s};$ $E_v = 73.3\text{ J/mm}^3$	$P=300\text{ W}; \nu=1000\text{ mm/s};$ $E_v = 95.2\text{ J/mm}^3$
d (μm)	57.2	64.9	118	193
w (μm)	98.5	113	135	169
L_b (μm)	156	237	522	1255
λ (μm)			105	
h (μm)			30	
$\%O_vR$	-6.6%	7.1%	22.2%	38.0%
$\%RD$	96.24	98.68	99.40	99.20
$\alpha/2$ $^\circ$	28.9	26.2	20.0	11.5
$\beta/2$ $^\circ$	25.0	20.3	8.8	3.9
$(\alpha/2 + \beta/2)$ $^\circ$	53.8	46.5	28.8	15.4
D_f	2.75	2.70	2.44	2.34

4 Conclusions

In this work, samples of Nb-48Ti produced by the LPBF-AM process were analyzed by profilometry, and the results obtained (fractal dimension and molten pool semi-angles) together with the previous characterization parameters (dimensions of the molten pool and relative density of the samples) indicate the potential of using surface characterization to evaluate integrity parameters of metal products obtained by this process.

It was also possible to describe the variation of the molten pool geometry through its solidification front edge asymmetrical semi-angles as seen in the XY plane and associate them with the overlapping generated by laser scanning during manufacturing. Both correlation results obtained between roughness (D_f) and molten pool border semi-angles ($\alpha/2$ and $\beta/2$) with LPBF volumetric energy (E_v) and overlapping ($\%O_vR$) are supported by the literature.

In addition, the present work demonstrated the potential of using this type of technique to describe better the three-dimensional geometry of the molten pool, including

the presentation of a simple 3D simulation. This possibility is exciting, as the properties of an LPBF-AM product, including its crystalline texture, strongly depend on the molten pool geometry.

Acknowledgements

The authors acknowledge the Companhia Brasileira de Metalurgia e Mineração (CBMM), Fundação de Amparo à Pesquisa do Estado de São Paulo (FAPESP) for their financial support (process number 2016/50199-6), Instituto de Pesquisas Tecnológicas (IPT), and Instituto Senai de Inovação em Sistemas de Manufatura e Processamento a Laser. F. J. G. Landgraf thanks to the support of the CNPq (grant 308991/2022-2), I. F. Machado thanks to the support of the CNPq (grant 305343/2022-0) and W. A. Morais, thanks to Mr. Fábio do Nascimento of the Surface Phenomena Laboratory (LFS-EPUSP) and to Dr. Daniel Luiz Rodrigues Junior of the LabMicro (PTM-EPUSP) for the kindly collaboration to this work.

References

- 1 DebRoy T, Wei HL, Zuback JS, Mukherjee T, Elmer JW, Milewski JO, et al. Additive manufacturing of metallic components - process, structure, and properties. *Progress in Materials Science*. 2018; 92:112-224. <https://doi.org/10.1016/j.pmatsci.2017.10.001>.
- 2 Khairallah SA, Anderson AT, Rubenchik A, King WE. Laser powder-bed fusion additive manufacturing: Physics of complex melt flow and formation mechanisms of pores, spatter, and denudation zones. *Acta Materialia*. 2016;108:36-45. <http://dx.doi.org/10.1016/j.actamat.2016.02.014>.
- 3 Gibson I, Rosen DW, Stucker B. *Additive manufacturing technologies: rapid prototyping to direct digital manufacturing*. New York (USA): Springer; 2010.
- 4 Brandt M. *Laser additive manufacturing*. Duxford (UK): Woodhead Publishing; 2017.
- 5 Reijonen J, Revuelta A, Riipinen T, Ruusuvoori K, Puukko P. The effect of shielding gas flow on porosity and melt pool geometry in laser powder bed fusion additive manufacturing. *Additive Manufacturing*. 2020;32:1-10. <http://dx.doi.org/10.1016/j.addma.2019.101030>.

- 6 Sun SH, Hagihara K, Nakano T. Effect of scanning strategy on texture formation in Ni-25at.%Mo alloys fabricated by selective laser melting. *Materials & Design*. 2018;140:307-316. <http://dx.doi.org/10.1016/j.matdes.2017.11.060>.
- 7 Mostafaei A, Ghiaasiaan R, Ho IT, Strayer S, Chang KC, Shamsaei N, et al. Additive Manufacturing of Nickel-based superalloys: a state-of-the-art review on process-structure-defect-property relationship. *Progress in Materials Science*. 2023;136:101108. <https://doi.org/10.1016/j.pmatsci.2023.101108>.
- 8 Jadhav SD, Goossens LR, Kinds Y, Hooreweder BV, Vanmeensel K. Laser-based powder bed fusion additive manufacturing of pure copper. *Additive Manufacturing*. 2021;42:101990. <https://doi.org/10.1016/j.addma.2021.101990>.
- 9 Jadhav SD, Dadbakhsh S, Goossens L, Kruth J-P, Van Humbeeck J, Vanmeensel K. Influence of selective laser melting process parameters on texture evolution in pure copper. *Journal of Materials Processing Technology*. 2019;270:47-58. <http://dx.doi.org/10.1016/j.jmatprotec.2019.02.022>.
- 10 Andreau O, Koutiri I, Peyre P, Penot JD, Saintier N, Pessard E, et al. Texture control of 316L parts by modulation of the melt pool morphology in selective laser melting. *Journal of Materials Processing Technology*. 2019;264:21-31. <http://dx.doi.org/10.1016/j.jmatprotec.2018.08.049>.
- 11 Morais WA, Landgraf FJG. Crystallographic texture configured by laser powder bed fusion additive manufacturing process: a review and its potential application to adjust mechanical properties of metallic products. *Tecnologica em Metalurgia, Materiais e Mineração*. 2023;20:1-12. <http://dx.doi.org/10.4322/2176-1523.20222802>.
- 12 Dai D, Gu D. Tailoring surface quality through mass and momentum transfer modeling using a volume of fluid method in selective laser melting of TiC/AlSi10Mg powder. *International Journal of Machine Tools & Manufacture*. 2015;88:95-107. <http://dx.doi.org/10.1016/j.ijmactools.2014.09.010>.
- 13 Mostafaei A, Zhao C, He Y, Ghiaasiaan SR, Shi B, Shi S, et al. Defects and anomalies in powder bed fusion metal additive manufacturing. *Current Opinion in Solid State and Materials Science*. 2022;26(2):100974. <http://dx.doi.org/10.1016/j.cossms.2021.100974>.
- 14 Vrancken B. Study of residual stresses in selective laser melting [thesis]. Leuven (Belgium): KU Leuven - Faculty of Engineering Science; 2016.
- 15 Guzmán J, Nobre RM, Rodrigues DL Jr, Morais WA, Nunes ER, Bayerlein DL, et al. Comparing spherical and irregularly shaped powders in laser powder bed fusion of Nb47Ti alloy. *Journal of Materials Engineering and Performance*. 2021;30:6557-6567. <http://dx.doi.org/10.1007/s11665-021-05916-9>.
- 16 Fundação de Amparo à Pesquisa do Estado de São Paulo - FAPESP. Fellowship Opportunities - PD Fellowships in Additive Manufacturing, FAPESP process number: 2016/50199-6, Project title: Obtenção de próteses ortopédicas de ligas Nb-Ti e Ti-Nb-Zr por fusão seletiva a laser [cited 2022 Apr 18]. Available at: https://www.fapesp.br/opportunidades/obtencao_de_protases_ortopedicas_de_ligas_nb-ti_e_ti-nb-zr_por_fusao_seletiva_a_laser/1721/
- 17 Subramanian S, Mohanty S, Prashanth KG. Effect of process parameters on the properties of β -Ti-Nb-based alloys fabricated by selective laser melting: a review. *Materials Today: Proceedings*. 2023. In press. <http://dx.doi.org/10.1016/j.matpr.2023.03.461>.
- 18 Hernández JSG. Análises microestruturais e mecânica da liga Ti-53%Nb produzida por fusão seletiva a laser usando pós esféricos e irregulares [dissertação]. São Paulo: Universidade de São Paulo; 2019. <https://doi.org/10.11606/D.3.2020.tde-21042020-100214>.
- 19 Nobre RM. Influência dos parâmetros do processo de manufatura aditiva de fusão em leito de pó na microestrutura e textura cristalográfica da liga Nb-47Ti [dissertação]. São Paulo: Universidade de São Paulo; 2021. <https://doi.org/10.11606/D.3.2021.tde-10082021-153818>.
- 20 Nobre RM, Morais WA, Vasques MT, Guzmán J, Rodrigues DL Jr, Oliveira HR, et al. Role of laser powder bed fusion process parameters in crystallographic texture of additive manufactured Nb-48Ti alloy. *Journal of Materials Research and Technology*. 2021;14:484-495. <http://dx.doi.org/10.1016/j.jmrt.2021.06.054>.
- 21 Balbaa M, Mekhail S, Elbestawi M, McIsaa J. On selective laser melting of Inconel 718: densification, surface roughness, and residual stresses. *Materials & Design*. 2020;193:108818. <http://dx.doi.org/10.1016/j.matdes.2020.108818>.
- 22 Ishimoto T, Wu S, Ito Y, Sun SH, Amano H, Nakano T. Crystallographic orientation control of 316L austenitic stainless steel via selective laser melting. *ISIJ International*. 2020;60(8):1758-1764. <http://dx.doi.org/10.2355/isijinternational.ISIJINT-2019-744>.
- 23 Majeed A, Ahmed A, Salam A, Muhammad ZS. Surface quality improvement by parameters analysis, optimization and heat treatment of AlSi10Mg parts manufactured by SLM additive manufacturing. *International Journal of Lightweight Materials and Manufacture*. 2019;2(4):288-295.

- 24 Malekipour E, El-Mounayri H. Common defects and contributing parameters in powder bed fusion AM process and their classification for online monitoring and control: a review. *International Journal of Advanced Manufacturing Technology*. 2018;95:527-550. <http://dx.doi.org/10.1007/s00170-017-1172-6>.
- 25 Di W, Yongqiang Y, Xubin S, Yonghua C. Study on energy input and its influences on single-track, multi-track, and multi-layer in SLM. *International Journal of Advanced Manufacturing Technology*. 2012;58(2):1189-1199. <http://dx.doi.org/10.1007/s00170-011-3443-y>.
- 26 Yang J, Fangzhi L, Aiqiong P, Huihui Y, Chunyang Z, Wenpu H, et al. Microstructure and grain growth direction of SRR99 single-crystal superalloy by selective laser melting. *Journal of Alloys and Compounds*. 2019;808:151740. <http://dx.doi.org/10.1016/j.jallcom.2019.151740>.
- 27 Darvish K, Chen ZW, Phan MAL, Pasang T. Selective laser melting of Co-29Cr-6Mo alloy with laser power 180–360 W: cellular growth, intercellular spacing and the related thermal condition. *Materials Characterization*. 2018;135:183-191. <http://dx.doi.org/10.1016/j.matchar.2017.11.042>.
28. Yadroitsev I, Smurov I. Selective laser melting technology: From the single laser melted track stability to 3D parts of complex shape. *Physics Procedia*. 2010; 5(B):551-560. <https://doi.org/10.1016/j.phpro.2010.08.083>.
- 29 Zhang C, Zhou Y, Wei K, Yang Q, Zhou J, Zhou H, et al. High cycle fatigue behaviour of Invar 36 alloy fabricated by laser powder bed fusion. *Virtual and Physical Prototyping*. 2023;18(1):e2190901. <http://dx.doi.org/10.1080/17452759.2023.2190901>.
30. Saghaian SE, Nematollahi M, Toker G, Hinojos A, Moghaddam NS, Saedi S, et al. Effect of hatch spacing and laser power on microstructure, texture, and thermomechanical properties of laser powder bed fusion (L-PBF) additively manufactured NiTi. *Optics and Laser Technology*. 2022;149:107680. <https://doi.org/10.1016/j.optlastec.2021.107680>.
- 31 Luo X, Song T, Gebert A, Neufeld K, Kaban I, Ma H, et al. Programming crystallographic orientation in additive-manufactured beta-type titanium alloy. *Advancement of Science*. 2023;10(28):2302884. <https://doi.org/10.1002/adv.202302884>.
- 32 Morais WA, Hernández JSG, Machado IF, Landgraf FJG. Study of the molten pool size of a Nb-48Ti alloy produced by laser powder bed fusion additive manufacturing. In: *Brazilian Metallurgy, Materials and Mining Association. Proceedings 76th ABM Annual Congress – International; 2023 August 1-3; São Paulo, Brazil*. São Paulo: Blucher; 2023. p. 2493-2504. <https://doi.org/10.5151/2594-5327-40354>.

Received: 24 Aug. 2023

Accepted: 7 Mar. 2024